

**Shock receptivity: characteristics of shock oscillation modes and induced boundary-layer disturbances**

CERMINARA, Adriano, LEVIN, Deborah A and THEOFILIS, Vassilios

Available from Sheffield Hallam University Research Archive (SHURA) at:

<https://shura.shu.ac.uk/32110/>

---

This document is the Accepted Version [AM]

**Citation:**

CERMINARA, Adriano, LEVIN, Deborah A and THEOFILIS, Vassilios (2023). Shock receptivity: characteristics of shock oscillation modes and induced boundary-layer disturbances. In: AIAA SCITECH 2023 Forum. Reston, VA, American Institute of Aeronautics and Astronautics. [Book Section]

---

**Copyright and re-use policy**

See <http://shura.shu.ac.uk/information.html>

# Shock receptivity: characteristics of shock oscillation modes and induced boundary-layer disturbances

Adriano Cerminara<sup>\*1</sup>, Deborah Levin<sup>†2</sup>, and Vassilis Theofilis<sup>‡3</sup>

<sup>1</sup>*University of Wolverhampton, Telford, TF2 9NT, United Kingdom*

<sup>2</sup>*University of Illinois at Urbana-Champaign, 104 S. Wright St. Urbana, IL 61801-2935, United States*

<sup>3</sup>*University of Liverpool, The Quadrangle, Liverpool L69 3GH, United Kingdom*

The shock layer represents a region of complex wave interaction phenomena, characterised by the presence of different types of disturbances, including both waves coming from the freestream as well as waves produced by molecular oscillations of the shock. The induced post-shock waves interact with the boundary layer and may cause generation and growth of additional instability modes. The waves associated with the inner shock molecular collisions have been recently demonstrated to be linked to a bimodal behaviour of the particle-energy probability distribution function (PDF) inside the shock, and to cover a low-frequency range. In the present contribution, direct numerical simulation (DNS) of the compressible flow governing equations<sup>15,21</sup> are performed to simulate oblique shock oscillations, within a range of Mach numbers ( $M = 2 - 6$ ), and at frequencies predicted by direct simulation Monte Carlo (DSMC) method,<sup>17</sup> as well as to study the characteristics of the resulting waves propagating in the shock layer and in the boundary layer. It is found that post-shock waves are radiated by the oscillating shock at the fundamental frequency, and that the interaction of these waves with the boundary layer generate modes with an amplified amplitude, including a progressive generation of higher harmonics of the fundamental wave as moving downstream. These, in turn, can synchronize with instability modes and promote their growth.

## I. Introduction

Transition to turbulence plays a crucial role on the heat-transfer rates on the surface of hypersonic vehicles, which makes it necessary to understand the physical mechanism responsible for transition, in order to allow accurate prediction of the transition location. The main path to transition, in the case of linear disturbances, can be summarized in three fundamental steps: i) receptivity, ii) modal growth of the instabilities and c) nonlinear instability and final breakdown to turbulence.

The way the boundary layer internalize the impinging disturbances from the upstream flow, in the form of internal instability modes, is crucial in the transition mechanism. In this context, the body leading edge is a highly-receptive zone, due to the non-parallel effects and the related short-scale streamwise variations of the mean flow, which, in turn, cause a wavelength-conversion process from the scale of the external forcing to that of the induced boundary-layer disturbances.<sup>1</sup> At hypersonic Mach numbers, however, it is well known that the small differences in phase speed between forcing waves and boundary-layer dominant modes lead to a direct excitation of these modes via a resonance mechanism at the leading edge,<sup>2-5</sup> without the need of a wavelength-conversion mechanism. Several numerical studies on the role of different types of freestream disturbances, particularly fast and slow acoustic waves, in the above-mentioned resonance mechanism have been carried out,<sup>4,9-15</sup> which highlighted the complex wave interaction features of the leading-edge receptivity, the synchronisation with the external forcing, downstream modulation and evolution of different induced

---

<sup>\*</sup>Lecturer in Aerospace Engineering, AIAA Member

<sup>†</sup>Professor of Aerospace Engineering

<sup>‡</sup>Professor of Aerospace Engineering

boundary-layer modes, whose type and relative significance in the transition process depend on the types and characteristics of the external impinging disturbances.

However, another receptive region of the flow is represented by the shock, whose susceptibility to external as well as wall-reflected waves and to inner molecular collisions is a source of additional wave modes that propagate within the shock layer and impinge onto the boundary layer, thus modulating the whole boundary-layer receptivity process. The role of the shock as an active source of instability modes within the boundary layer has received substantially less attention in the literature, and deserves careful attention in the study of the physical mechanism of transition, as different transition scenarios can occur dependent on the characteristics disturbances radiated in the post-shock region from an oscillating shock.

A recent DSMC study has identified for the first time spanwise-periodic linear modal instabilities inside the separation and reattachment shock layers associated with SLBLI on a three-dimensional double wedge.<sup>16</sup> These instabilities are synchronized in frequency and have identical spanwise wavelength with the well-known self-excited three-dimensional global mode of the underlying laminar separation bubble. Furthermore, the correlation between the shock bimodality and the formation of low-frequency oscillations was demonstrated<sup>17</sup> and analyzed in detail.<sup>18</sup> The bimodality behaviour is associated with the molecular nonequilibrium state inside the shock, which causes a bimodal shape of the probability distribution function (PDF) associated with two streams of molecular energies. Within the shock, the PDF peaks at two different energy values, corresponding to collisions between molecules upstream and downstream of the shock. These in turn will cause waves that are transmitted from the shock into the downstream (post-shock) flow field. This type of additional forcing due to kinetic fluctuations of the shock belongs to the category of “stochastic forcing”, emphasised by Fedorov and Tumin<sup>19</sup> as responsible for the generation of unstable boundary-layer modes which undergo a significant amplification toward the nonlinear region and can lead to transition to turbulence. This behaviour was observed in DSMC studies of Tumuklu et al.<sup>20</sup> for the unsteady flow over a double cone.<sup>20</sup> Sawant et al.<sup>17</sup> developed an analytical model based on non-central chi-squared (NCCS) distributions to reproduce the bimodal PDF of the particle energy inside a normal shock. The analytical model was found to agree well with the actual distribution obtained from DSMC simulations. Moreover, the analytical PDF have been used to correlate the shape of the PDF to the DSMC-derived low fluctuation frequencies, in a Mach number range from 3 to 10, and in a temperature range from 89 K to 1420 K, showing a linear proportionality of the DSMC-derived low frequencies of the oscillations with the location of the PDF peak in energy space.

Contextually, in the DNS of Cerminara and Sandham<sup>21</sup> for the flow over a swept wedge a previously unseen transition mechanism has been found, which is associated with the generation at the leading edge and downstream growth of a high-spanwise wavenumber mode, whose source has been found correlated with a shock-wall wave reflection mechanism. This demonstrates that oscillations radiated from the shock can induce early transition in hypersonic flow. Moreover, in the study of Klothakis et al.,<sup>22</sup> induced shock oscillations in DSMC simulations have been found synchronized with boundary layer disturbances analysed through linear stability analysis (LST).

The present study is aimed at the analysis of the shock oscillation modes and the wave characteristics of the radiated disturbance field in the shock layer, at different Mach numbers, as well as the analysis of the correlated effects on the boundary-layer receptivity process and the induced instability modes. DNS simulations are performed for different oblique oscillating shock configurations, with imposed oscillation frequencies obtained through DSMC simulations. In addition, LST analysis is carried out within the boundary layer to identify the local unstable modes, and compare them with the generated disturbances captured in the DNS. Results for the frequency spectra and Fast-Fourier-transformed pressure fluctuation distribution downstream of the shock and on the solid surface, as well as for the eigenfunctions and phase speed of the boundary-layer modes allow identification of the correlation between shock modes and boundary-layer modes in a complex combined shock-receptivity / boundary-layer receptivity phenomenon, and conclusions are drawn on the associated effects on the transition process.

## II. Numerical method

### II.A. Governing equations

We consider numerical solutions of the three-dimensional Navier-Stokes equations for compressible flows, written in conservation form, under the assumption of perfect gas. The set of non-dimensional conservation equations in Cartesian coordinates can be written as

$$\frac{\partial \mathbf{Q}}{\partial t} + \frac{\partial(\mathbf{F}_j)}{\partial x_j} = 0,$$

In the equation above,  $\mathbf{Q}$  is the vector of the conservative variables, while  $\mathbf{F}_j$  is the vector of the fluxes in Cartesian coordinates. The components of the vectors of the system in conservative form are

$$\mathbf{Q} = \begin{bmatrix} \rho \\ \rho u \\ \rho v \\ \rho w \\ \rho E \end{bmatrix},$$

$$\mathbf{F}_j = \begin{bmatrix} \rho u_j \\ \rho u u_j + \delta_{1j} p - \frac{1}{Re} \tau_{1j} \\ \rho v u_j + \delta_{2j} p - \frac{1}{Re} \tau_{2j} \\ \rho w u_j + \delta_{3j} p - \frac{1}{Re} \tau_{3j} \\ \rho \left( E + \frac{p}{\rho} \right) u_j - \frac{1}{Re} \left( u \tau_{1j} + v \tau_{2j} + w \tau_{3j} + \frac{\mu}{(\gamma - 1) Pr M^2} \frac{\partial T}{\partial x_j} \right) \end{bmatrix}$$

The terms  $\rho$ ,  $\rho u$ ,  $\rho v$ ,  $\rho w$  and  $\rho E$  are the conservative variables of the system of equations, where  $\rho$  is the density,  $u$ ,  $v$  and  $w$  are the velocity components respectively in the  $x$ ,  $y$  and  $z$  directions, and  $E$  is the total energy per unit mass. In the flux vectors, the terms  $p$ ,  $T$ ,  $\tau_{ij}$ , and  $\mu$  are respectively the pressure, the temperature, the components of the viscous stress tensor, and the dynamic viscosity of the flow. The non-dimensional quantities are obtained through normalisation of the dimensional variables with their freestream reference values: the velocity components are normalised with the freestream main velocity ( $U_\infty^*$ ), the density is normalised with the freestream density ( $\rho_\infty^*$ ), the viscosity is normalised with the freestream dynamic viscosity ( $\mu_\infty^*$ ), the temperature is normalised with the freestream temperature ( $T_\infty^*$ ), the total energy is normalised with the square of the freestream mean velocity ( $U_\infty^{*2}$ ), while the pressure and viscous stresses are normalised with the term  $\rho_\infty^* U_\infty^{*2}$ , related to the freestream dynamic pressure. Note that the superscript (\*) is used to denote dimensional values. The nose radius ( $R^*$ ) is chosen as the characteristic length to normalise the length scales, while the time scales are normalised with respect to the fluid dynamic characteristic time ( $R^*/U_\infty^*$ ), based on the velocity of the undisturbed flow and on the characteristic length. The terms  $Re$ ,  $Pr$ ,  $M$ , and  $\gamma$  are respectively the Reynolds, Prandtl and Mach numbers, and the ratio of specific heats ( $\gamma = c_p^*/c_v^*$ ), i.e. the dimensionless parameters of the flow. The Reynolds number is defined with respect to the nose radius, as  $Re = (\rho_\infty^* U_\infty^* R^*)/\mu_\infty^*$ ; the Prandtl number is set to 0.72 for air, and  $\gamma$  is equal to 1.4, as we are considering a perfect gas model. The dynamic viscosity is, in turn, expressed in terms of temperature by Sutherland's law

$$\mu = T^{3/2} \frac{1 + C}{T + C},$$

where the constant  $C$  represents the ratio between the Sutherland's constant (set to 110.4 K) and the reference temperature ( $T_\infty^*$ ). The viscous stresses are defined in terms of the velocity derivatives, under the assumption of a Newtonian fluid, as

$$\tau_{ij} = \mu \left[ \frac{\partial u_i}{\partial x_j} + \frac{\partial u_j}{\partial x_i} - \frac{2}{3} \delta_{ij} \frac{\partial u_k}{\partial x_k} \right].$$

We also need a relation linking the total energy to the temperature, which in non-dimensional form can be expressed as

$$E = \frac{T}{\gamma(\gamma - 1)M^2} + \frac{1}{2} (u^2 + v^2 + w^2) .$$

Finally, the system of equations is closed by the equation of state for a perfect gas

$$p = \frac{1}{\gamma M^2} \rho T .$$

The system of equations in Cartesian coordinates is transformed into a system of equations in curvilinear coordinates ( $\xi, \eta, \zeta$ ) as

$$\frac{\partial \bar{\mathbf{Q}}}{\partial t} + \frac{\partial (\bar{\mathbf{F}}_j)}{\partial \xi_j} = 0.$$

The relations between the vectors in curvilinear and Cartesian coordinates are expressed by

$$\bar{\mathbf{Q}} = J \mathbf{Q}, \quad \bar{\mathbf{F}}_j = J \mathbf{F}_i \frac{\partial \xi_j}{\partial x_i},$$

with  $J = \det \|\partial(x, y, z)/\partial(\xi, \eta, \zeta)\|$  being the jacobian of the transformation matrix.

The code used to carry out the numerical simulations is SBLI (Shock-Boundary-Layer-Interaction), developed over a number of years at the University of Southampton, consisting of a 4<sup>th</sup>-order central differencing scheme, as base scheme, in conjunction with a 2<sup>nd</sup>-order Harten-Yee TVD (Total-Variation-Diminishing) shock-capturing scheme,<sup>23</sup> as a filter step. A validation of the code can be found in De Tullio *et al.*<sup>24</sup>

### III. Results

#### III.A. Mach 2, frequency spectrum $f_1$ to $f_5$

Numerical simulations have been performed on a 2D flat-plate domain, for a Mach 2 flow with Reynolds number of 950, based on the boundary-layer displacement thickness at the inlet boundary, freestream temperature of 288 K, and for an adiabatic wall. The present flow conditions are representative of conditions in the simulations of Katzer<sup>25</sup> for shock/boundary-layer interaction cases. The flow is initialised with the similarity solution for the boundary layer, an extrapolation boundary condition is used at the inlet boundary, and an isothermal no-slip wall condition is set on the bottom boundary, with a nondimensional temperature of  $T_w = 1.676$ , corresponding to the adiabatic temperature condition of the similarity solution. At the inlet

boundary, a shock generator, based on the Rankine-Hugoniot jump conditions, is imposed outside of the boundary layer to simulate an oblique shock generated through a half-wedge (or deviation) angle of  $10.5^\circ$ , which propagates downstream. After a steady state condition is reached, shock oscillations are imposed by moving the shock generator upwards and downwards following a sinusoidal profile with time, at specified frequencies corresponding to the frequencies predicted in the DSMC of Sawant et al.<sup>17</sup> In particular, five frequencies have been considered, namely  $f_1 = 13$  kHz,  $f_2 = 18$  kHz,  $f_3 = 23$  kHz,  $f_4 = 25$  kHz, and  $f_5 = 34$  kHz. The domain size is  $L_x = 200$  and  $L_y = 115$ , and the grid size is  $N_x \times N_y = 401 \times 251$ . A stretching function is used in the  $y$ -direction for grid point clustering towards the wall in order to accurately resolve the boundary layer.

Figure 1 provides an overview of the flowfield qualitative features. As can be seen, the oblique shock wave is oscillating, generating post-shock wave fronts which propagate downstream perturbing the boundary layer. Figures 2, 3, 4 show the Fast-Fourier-transformed pressure fluctuation frequency spectra and streamwise distribution on the wall and downstream of the shock. The frequency spectra have been extracted at a probe in the post-shock region and at three different positions on the wall. Whereas, the streamwise pressure fluctuation amplitude distributions have been extracted on the wall ( $y = 0$ ) and along an horizontal line at the height  $y = 30$ . It can be observed that, both on the wall and in the shock layer, the most amplified waves are those at the fundamental frequency, as expected. However, a progressive generation of higher harmonics is observed as well, moving downstream along the wall. The generation of higher harmonics is more pronounced at the higher imposed frequencies, and the downstream flow regions are characterised by the generation of harmonics at increasing frequency. The pressure fluctuation distributions show that the wall response is amplified compared to the post-shock response through the whole length, and that a modulation process is present between different competing modes, both within the shock layer and within the boundary layer, which is characterised by a bumping behaviour of the distribution profiles. The characteristic wavelength of this modulation process is different between the waves in the shock layer and in the boundary layer, thus suggesting that different additional modes generate and are evolving inside the boundary layer.

The boundary-layer response to the highest frequency,  $f_5 = 34$  kHz, shown in figure 4, reveals the origin of a higher frequency mode corresponding to the fifth harmonic, at about 175 kHz, in the downstream region, which has a higher amplitude compared to the lower-frequency higher harmonics, and which is not present at the lower frequencies. Figure 5 shows the streamwise distribution of the signal phase speed associated with the pressure fluctuations on the surface, which reveals that the wall response at the highest frequency ( $f_5$ ) approaches the value of 0.5, representing the phase speed of slow acoustic waves in the present case. Hence, this suggests that a synchronisation process with the slow mode (or mode S) is present within the boundary layer with resulting generation and downstream development of the slow mode, which may be at the basis of the amplification of the higher frequency mode observed in the corresponding frequency spectrum. Finally, figure 6 shows the amplification factor of the wall response with respect to the disturbance level in the post-shock region, computed as ratio between the peak amplitude of the Fast-Fourier-transformed wall pressure fluctuations and the corresponding average amplitude level in the post-shock region, for the different fundamental frequencies of the shock oscillations. The profile shows that the amplification factor increases rapidly at increasing frequency of the shock oscillations, for the first four frequencies, reaching a maximum of about 10 at the frequency  $f_4$ , whereas it slightly decreases to about 9.5 at the frequency  $f_5$ . This demonstrates that shock oscillations can induce disturbances in the boundary layer higher by an order of magnitude compared to those radiated in the post-shock region, with amplification factor increasing with the frequency.

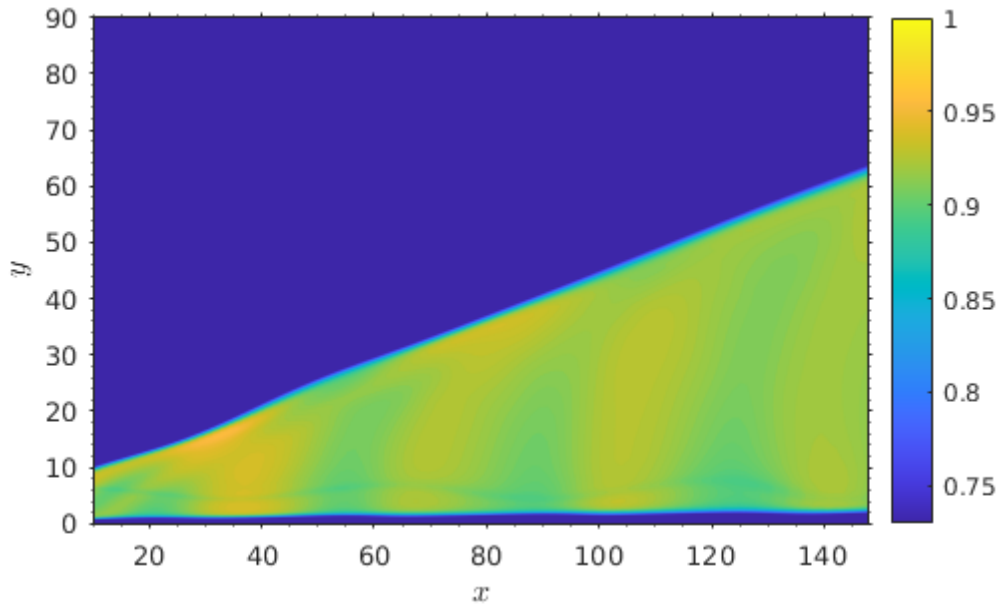


Figure 1: Instantaneous density field, with evidence of wave fronts radiated from the oscillating shock and interacting with the boundary layer

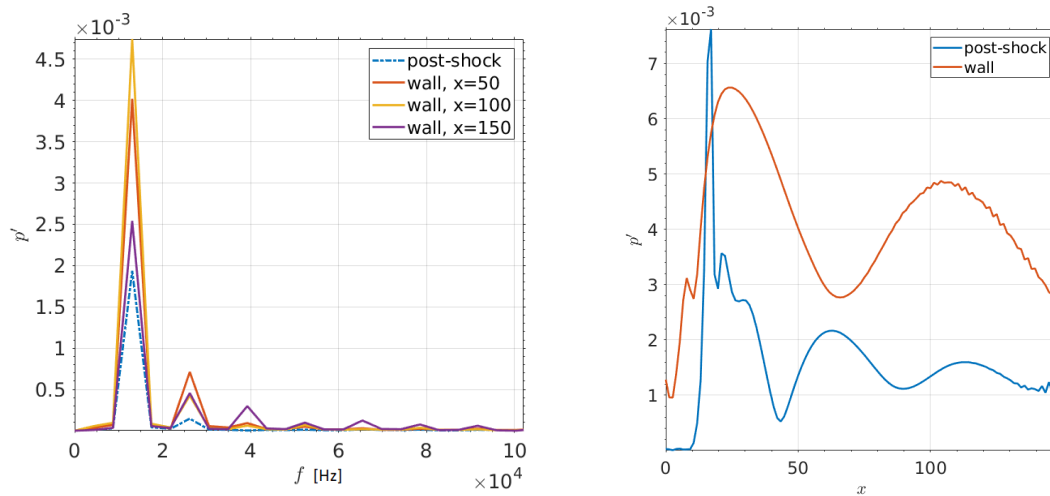


Figure 2: Frequency spectrum (left) and distribution of pressure fluctuation amplitude (right) on the surface and downstream of the shock, for the frequency  $f_1$

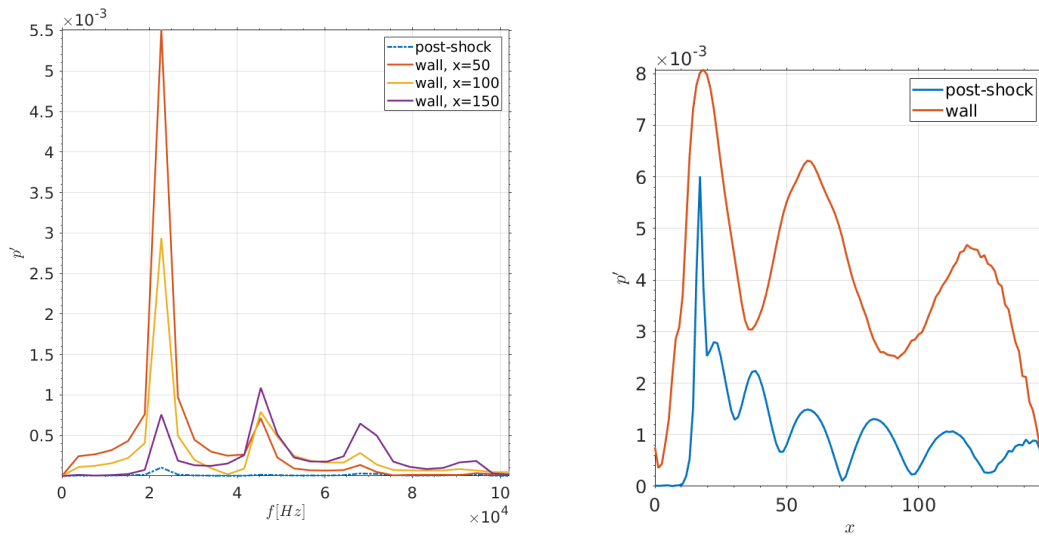


Figure 3: Frequency spectrum (left) and distribution of pressure fluctuation amplitude (right) on the surface and downstream of the shock, for the frequency  $f_3$

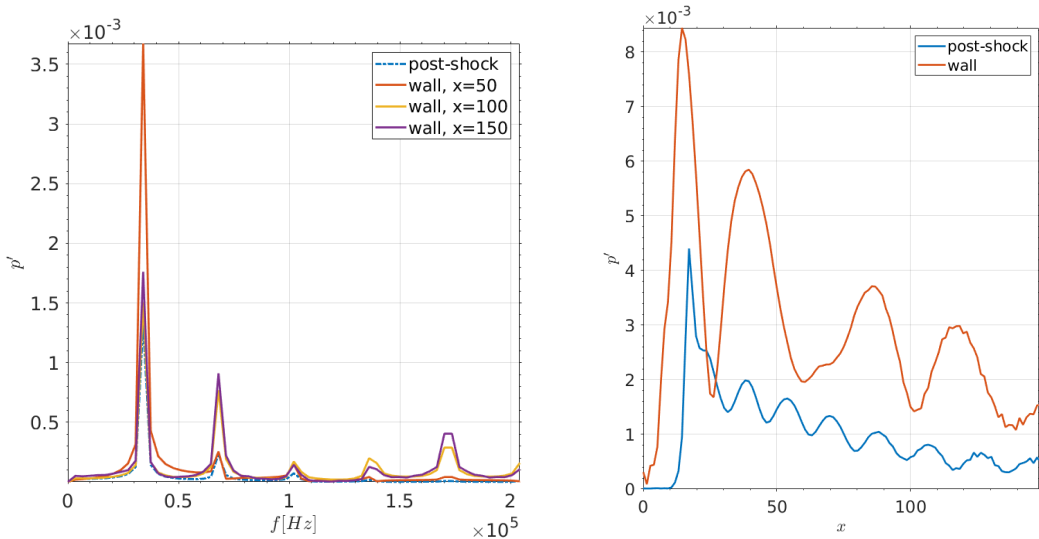


Figure 4: Frequency spectrum (left) and distribution of pressure fluctuation amplitude (right) on the surface and downstream of the shock, for the frequency  $f_5$

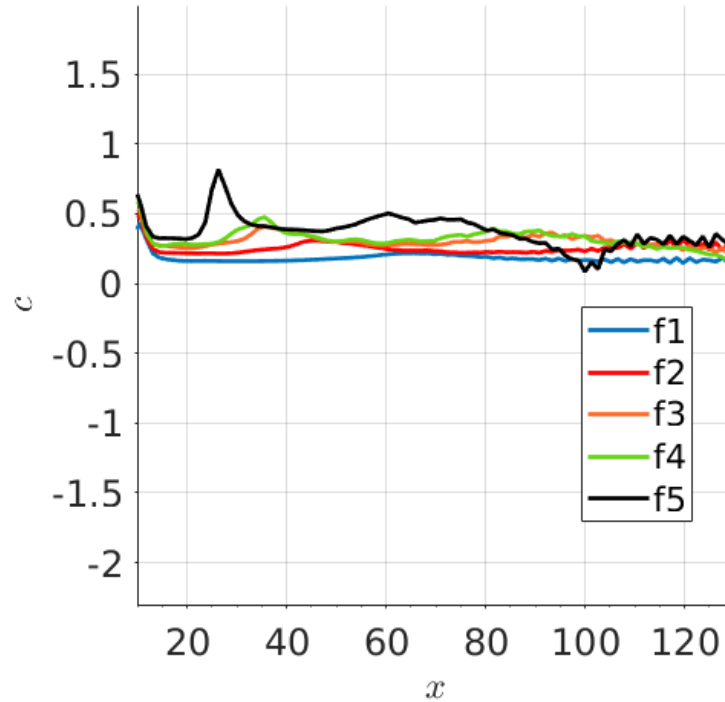


Figure 5: Phase speed associated with the different pressure fluctuation signals representing the wall response at the different frequencies of the shock oscillations

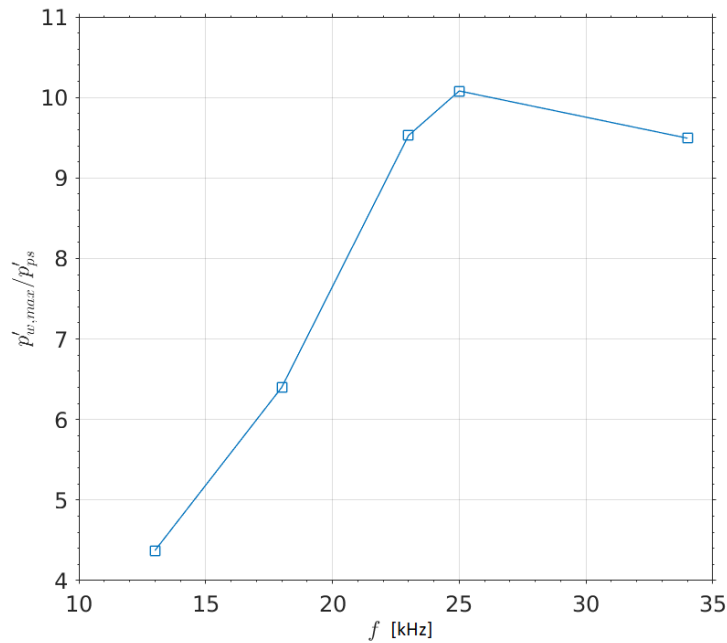


Figure 6: Amplification factor (wall-to-post-shock pressure fluctuation amplitude ratio) of the wall response with respect to the shock layer response

### III.B. Mach 3, frequency $f_1$

We now increase the Mach number, keeping constant the Reynolds number and freestream temperature as in III.A. The wall is considered as adiabatic. In the work of Sawant et al.,<sup>17</sup> the flows associated with an

evident bimodal behaviour are those at higher Mach number, i.e. for  $M \geq 3$ . In this section we consider the smallest Mach number for which a bimodal profile of the molecular energy PDF was found in,<sup>17</sup> i.e. Mach 3. At this Mach number, Sawant et al.<sup>17</sup> predicted a frequency of 13 kHz ( $f_1$ ) for the shock oscillations arising from the shock bimodality. Hence, we impose oscillations of the Mach 3 oblique shock at 13 kHz.

Figures 7 and 8 show frequency spectra at different positions over the surface and on a probe in the post-shock region (in figure 7) with coordinates  $x = 100$  and  $y = 10$ . As can be seen, a strong peak near 150 kHz is reached on the wall, which increases as moving further downstream. This frequency is not excited in the post-shock region, but becomes the dominant frequency downstream of  $x = 100$ , with the amplitude reaching a value of 0.045, which is higher than the amplitude of the fundamental frequency by a factor of 2.25. The excitation of this high-frequency unstable mode at relatively high amplitude values is responsible for a nonlinear growth of the disturbances in the downstream region. This can be better observed figures 9 and 10, for the contours of the pressure fluctuations and instantaneous temperature field, which show nonlinear waves originating near  $x = 100$  and developing downstream producing strong oscillations of the boundary layer. In figure 9 it is also possible to observe the pressure fluctuations located on the oscillating oblique shock wave.

Figure 11 shows a comparison of the pressure fluctuation amplitude downstream of the shock and on the wall for the fundamental frequency ( $f_1$ ). It should be mentioned that the  $x$ -axis is representative of the distance on the surface from the inlet boundary, however the pressure fluctuation amplitude downstream of the shock is plotted along a horizontal line at the height  $y = 10$  within the computational domain, and is shifted by  $\Delta x = 50$  backwards along the  $x$ -direction such to show the points from the immediate downstream region of the shock. We can observe that in this case the response of the shock layer and the response of the wall to the shock oscillations at the imposed frequency is comparable in amplitude, with an amplification factor at the peak of the wall response of about 1.38 (ratio between peak of the wall response and mean amplitude level in the post-shock region). The lower value of the amplification ratio compared to the previous case at Mach 2, at the same frequency, can be addressed to the lower shock angle reached at higher Mach numbers (for the same half-wedge angle), which indicates the relevant role played by the shock angle on the amplification of the shock-oscillation-induced disturbances on the body surface.

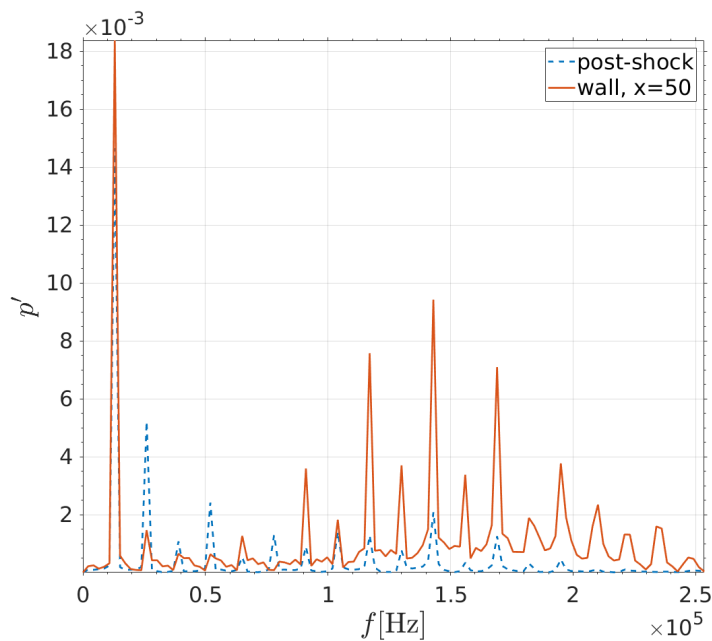


Figure 7: Frequency spectrum in the post-shock region and on the surface (at  $x = 50$ )

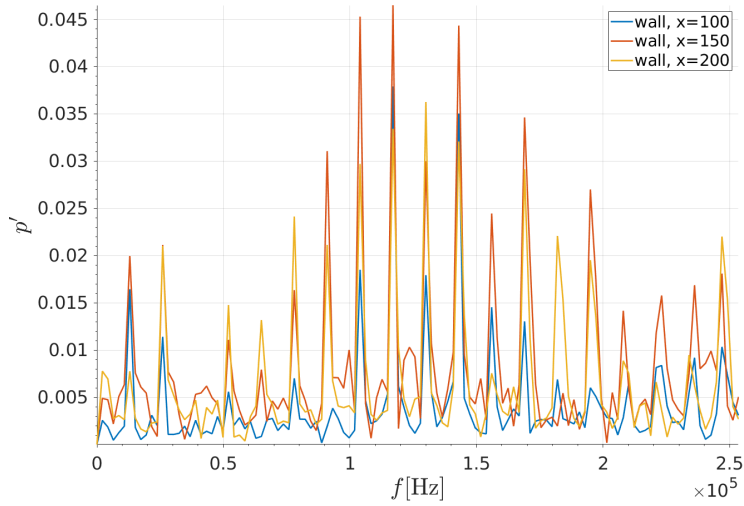


Figure 8: Frequency spectrum on the surface (downstream of  $x = 50$ )

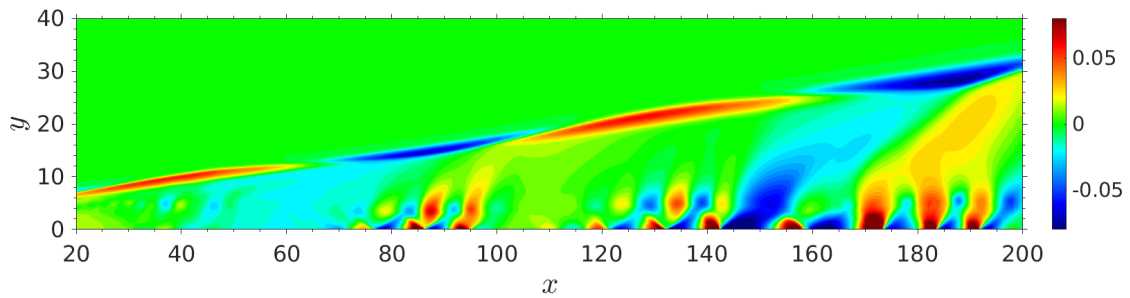


Figure 9: Pressure fluctuation contours downstream of the shock and in the boundary layer

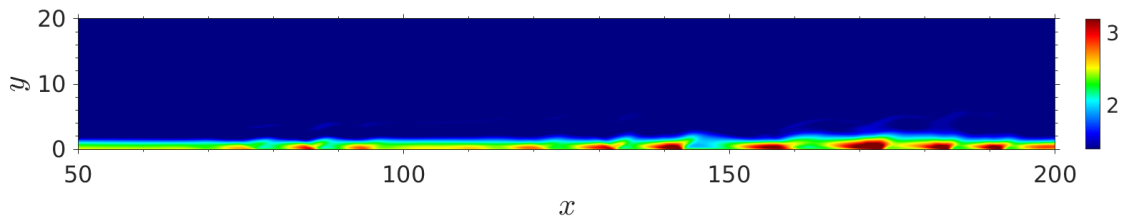


Figure 10: Instantaneous temperature field within the boundary layer with nonlinear disturbance growth in the downstream region

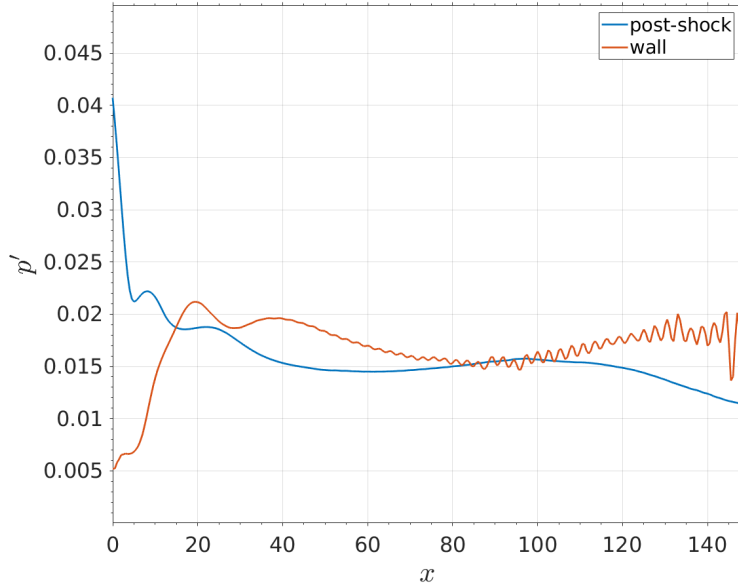


Figure 11: Pressure fluctuation amplitude in the post-shock region and on the surface, at the fundamental frequency

### III.C. Mach 5, frequency $f_3$

We now consider the DSMC-derived frequency by Sawant et al.<sup>17</sup> corresponding to Mach 5, i.e.  $f_3 = 23$  kHz. We simulate a Mach 5 boundary layer, with same Reynolds number and freestream temperature conditions as described in section III.A, and for an adiabatic wall. In this case, we impose a smaller half-wedge/deviation angle to generate the oblique shock, i.e.  $\delta = 3^\circ$ .

Figure 12 shows the frequency spectrum of the disturbances at a probe in the post-shock region ( $x = 100$ ,  $y = 10$ ) and at different positions over the surface. Circle markers are added here for the post-shock spectrum in order to help identify it among the other modes. Although the Mach number is higher than in the previous cases, the oblique shock is relatively weaker due to the significantly smaller deviation angle. This can be observed by considering the smaller highest amplitude (for the positions shown in the graph) reached at the fundamental frequency ( $4.5 \times 10^{-3}$ ), compared to e.g. the corresponding graph for the Mach 3 case in figure 7 ( $1.8 \times 10^{-3}$ ). Moreover, it can be seen that for the Mach 5 case the fundamental frequency is the dominant frequency over the whole wall length, with the frequency spectrum in 12 showing a gradually decreasing amplitude reached at the higher frequencies. However, it is interesting to notice that, among the higher frequencies, the second, fourth and sixth higher harmonics are the most amplified and within the order of magnitude of the fundamental frequency. This suggests that an internal wave modes with the second multiple integer with respect to the fundamental frequency is excited from the shock-induced oscillations, along with its higher harmonics. In figure 13 contours of the pressure fluctuations are shown, which highlight the wave patterns along the oblique shock, within the shock layer and in the boundary layer. The main wave pattern transmitted into the boundary layer is the same as the dominant wave pattern in the shock layer, and represents the fundamental frequency. However, some smaller wavelength disturbances can be seen to originate and develop downstream. Figure 14 show the comparison between the Fast-Fourier-transformed pressure fluctuation amplitude in the post-shock region (shifted upstream by  $\Delta x = 50$ ) and on the wall, at the fundamental frequency. It can be observed that as soon as the wall is reached by the waves radiated from the shock the amplitude rapidly increases to a value just below  $5 \times 10^{-3}$ , which is close to the amplitude in the shock layer, and shows a streamwise distribution similar to the corresponding profile in the post-shock region. Hence the wall response appears similar to the shock-layer response at the fundamental frequency, and the absence of pronounced bumps/oscillations in the profiles indicates that both shock layer and boundary layer are dominated by the fundamental frequency mode of the shock oscillations. For this case a wall-to-post-shock amplification factor of 1.24 has been obtained at the peak of the wall response.

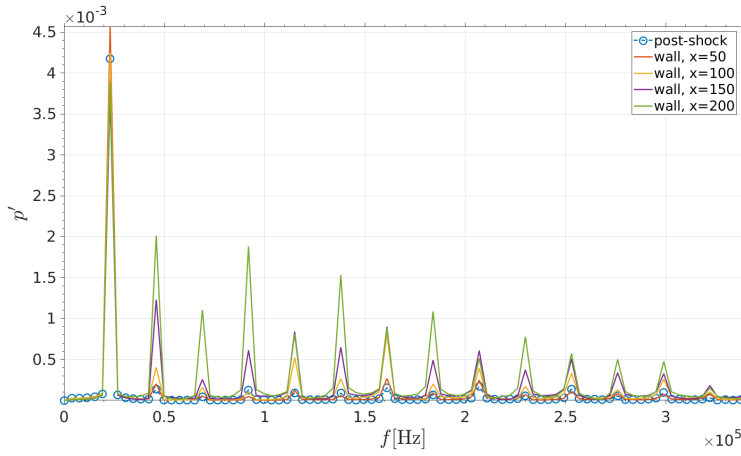


Figure 12: Frequency spectrum in the post-shock region and on the surface

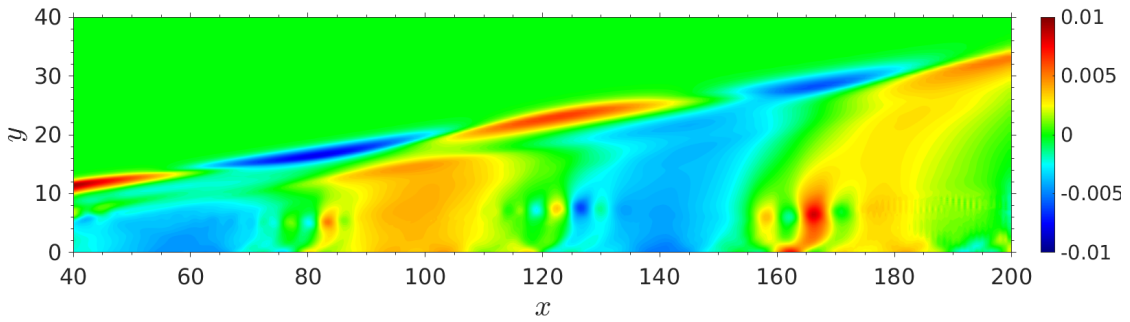


Figure 13: Pressure fluctuation contours downstream of the shock and in the boundary layer

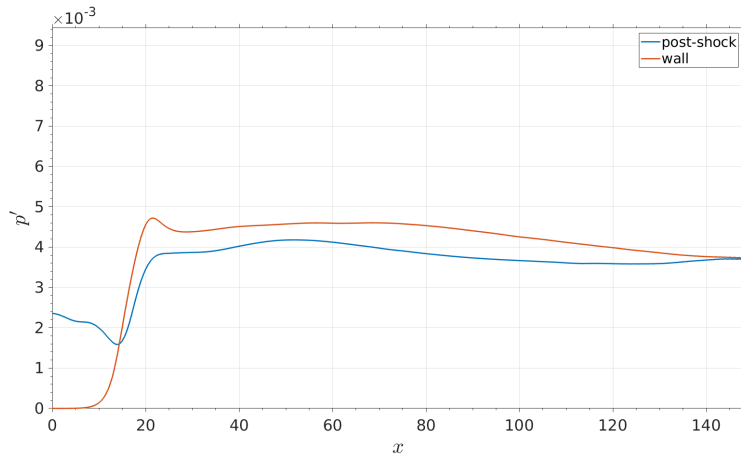


Figure 14: Pressure fluctuation amplitude in the post-shock region and on the surface, at the fundamental frequency

### III.D. Mach 6, frequency $f_4$

Finally, we consider a Mach 6 flow and the corresponding DSMC-derived frequency by Sawant et al.,<sup>17</sup> i.e.  $f_4 = 25$  kHz. Again, Reynolds number and freestream temperature conditions are the same as those in section III.A, and the wall is considered as adiabatic. Similarly to the Mach 5 case, we impose a deviation angle  $\delta = 3^\circ$  to generate the oblique shock.

Figure 15 shows the frequency spectrum of the disturbances at a probe in the post-shock region ( $x = 100$ ,  $y = 10$ ) and at different positions over the surface. Similarly to the Mach 5 case, the fundamental frequency

is the dominant frequency over the whole length of the wall; the higher harmonics are present, but in a lower extent compared to the Mach 5 case.

The pressure fluctuation contours in figure 16 show similar patterns to the Mach 5 case, with the fundamental frequency transmitted by the oscillating shock dominating both the shock layer and the boundary layer. The profiles of the pressure fluctuation amplitude at the fundamental frequency in the shock layer and along the wall, in figure 17, are a further confirmation of the dominance of the fundamental frequency both downstream of the shock and on the wall, as well as of the similarity of the wave patterns with the Mach 5 case (as seen in figure 14). The disturbance amplitude on the wall is relatively close to that in the post-shock region, and a wall-to-post-shock amplification factor of 1.4 has been obtained at the peak of the wall response.

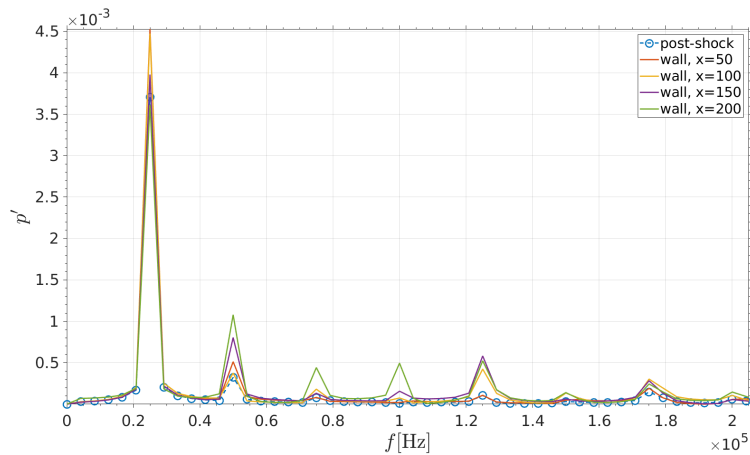


Figure 15: Frequency spectrum in the post-shock region and on the surface

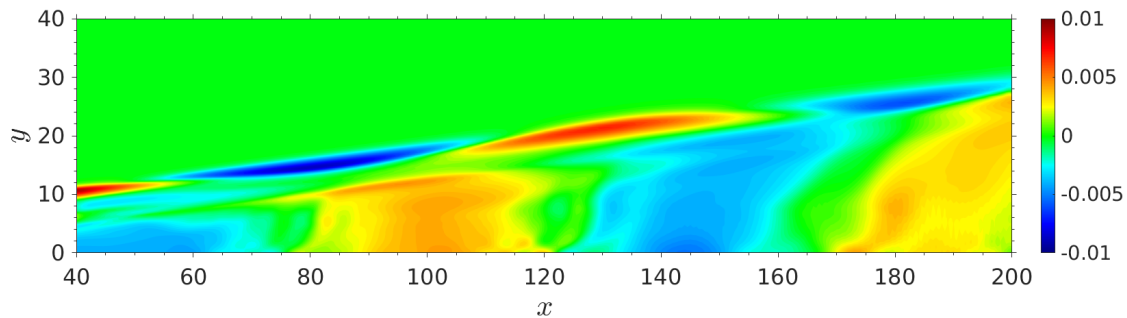


Figure 16: Pressure fluctuation contours downstream of the shock and in the boundary layer

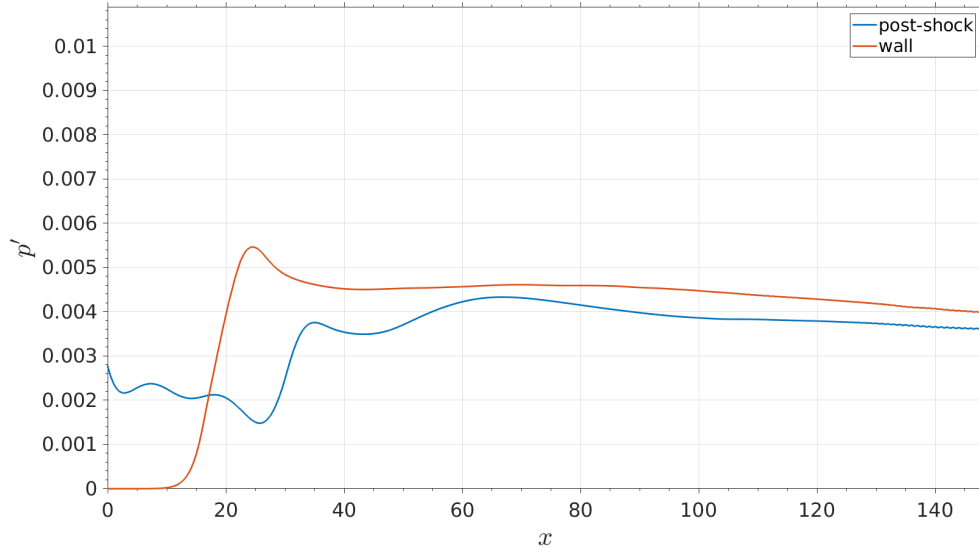


Figure 17: Pressure fluctuation amplitude in the post-shock region and on the surface, at the fundamental frequency

## IV. Conclusion

Direct numerical simulations have been performed for an oscillating oblique shock and for a boundary layer over a flat plate, with imposed shock oscillation frequencies corresponding to those obtained in a reference DSMC study on the shock oscillations associated with the inner molecular nonequilibrium. Flows at Mach numbers 2, 3, 5 and 6 are considered, with an assigned half-wedge/deviation angle of the shock generator to induce an oblique shock, and assigned frequency of oscillations of the shock. An analysis of the receptivity to the shock-induced waves within the shock layer and the boundary layer allows identification of the dominant modes and their evolution, as well as comparison between the shock layer response and the wall response, when the DSMC predicted frequencies are imposed as fundamental frequencies for the shock oscillations. It is found that the shock oscillations at the different frequencies produce a post-shock disturbance field dominated by the fundamental frequency, and that the interaction of the post-shock waves with the boundary layer produces the generation and downstream evolution of higher harmonics. For all the Mach numbers, higher harmonics start developing at different positions along the surface, with an increasing multiple frequency as moving downstream.

At Mach 2, and for a deviation angle of  $10.5^\circ$ , the amplitude of the wall response appears significantly amplified compared to the disturbance level in the shock layer, with a maximum amplification factor of about 10 reached at the frequency  $f_4$ . Both the post-shock and wall pressure fluctuation streamwise distributions show evidence of a modulation behaviour that involves different competing modes. However, the modulation behaviour appears different in the characteristic bumping wavelength, suggesting that different additional modes are formed within the boundary layer. The highest frequency,  $f_5$ , shows evidence of downstream generation of a higher frequency mode, at about 175 kHz, absent in the lower frequency cases, which is characterised by the phase speed of the slow acoustic waves. This suggests the presence of a synchronisation mechanism with the slow mode (mode S) within the boundary layer, with resulting excitation and downstream evolution of a high-frequency boundary-layer mode.

At Mach 3, for the same deviation angle as the Mach 2 case, and for a shock-oscillation frequency of 13 kHz, which was found as the frequency associated with a shock at Mach 3 through DSMC, the frequency spectrum on the wall appears significantly different to the lower Mach number case. In particular, a strong excitation of high-frequency modes with peak at 150 kHz is observed in the downstream region, which is responsible for a rapid nonlinear growth of the disturbances and boundary-layer distortion. The wall-to-post-shock disturbance amplitude amplification ratio obtained at the peak of the wall response, for the fundamental frequency, is smaller than the values obtained for the Mach 2 case at different frequencies, which is considered to be an effect of the smaller oblique shock angle for the Mach 3 case.

The cases at Mach 5 and 6, for which a smaller deviation angle of  $3^\circ$  has been considered, show similar

wave patterns both in the shock layer and in the boundary layer. The fundamental frequency predicted by DSMC at both Mach numbers is the dominant frequency downstream of the shock and within the boundary layer, which is also demonstrated by the absence of a bumping/oscillatory behaviour (i.e. of a modulation pattern) of the pressure fluctuation profiles in both flow regions (which would be, in contrast, a sign of the presence of competing modes). The response on the wall appears slightly amplified compared to the amplitude of the shock layer response, with a higher amplification factor for the Mach 6 case. Higher harmonics generate and develops on the wall, but their magnitude is significantly lower than the amplitude of the fundamental frequency, with exception of three higher harmonics (of the second multiple integer), namely the second, fourth and sixth harmonics, in the Mach 5 case, which are within the same order of magnitude of the fundamental frequency, thus indicating generation and downstream evolution of higher frequency boundary-layer modes induced by the predicted DSMC shock-oscillation frequency.

The present work demonstrates that shock oscillations, at the natural frequencies associated with inner molecular oscillations, are an efficient route for the generation of disturbances within the shock layer and in the boundary layer, at the same fundamental frequency as well as at higher frequencies, which can potentially lead to instability excitation and downstream nonlinear growth. The study of such instability route is of great importance for the prediction of hypersonic transition, and should be subject of future investigation aimed at the study of the transition mechanism and the design of calibrated physics-based transition prediction methods.

## References

- <sup>1</sup>Saric, W., Reed, H., and Kerschen, E. *Boundary-layer receptivity to freestream disturbances*, Annual Review of Fluid Mechanics 34, 2002
- <sup>2</sup>Fedorov, A. V., and Khokhlov, A. P. *Prehistory of Instability in a Hypersonic Boundary Layer*, Theoretical and Computational Fluid Dynamics 14 (6), 2001
- <sup>3</sup>Fedorov, A. V. *Transition and Stability of High-Speed Boundary Layers*, Annual Review of Fluid Mechanics 43 (1), 2011
- <sup>4</sup>Zhong, X., and Ma, Y. *Boundary-layer receptivity of Mach 7.99 flow over a blunt cone to free-stream acoustic waves*, Journal of Fluid Mechanics, 556, 2006
- <sup>5</sup>Zhong, X., and Wang, X. *Direct Numerical Simulation on the Receptivity, Instability, and Transition of Hypersonic Boundary Layers*, Annual Review of Fluid Mechanics 44 (1), 2012
- <sup>6</sup>Mack, L. M. *Boundary-layer linear stability theory*, Tech. Rep., California Inst. of Technology, Pasadena JPL, 1984
- <sup>7</sup>Stetson, K. F., Thompson, E. R., Donaldson, J. C., and Siler, L. G. *Laminar boundary layer stability experiments on a cone at Mach 8. ii- blunt cone*, American Institute of Aeronautics and Astronautics, Aerospace Sciences Meeting 22nd, Reno, NV, 1984
- <sup>8</sup>Fedorov, A. V., Malmuth, N. D., Rasheed, A., and Hornung, H. G. *Stabilization of hypersonic boundary layers by porous coatings*, AIAA Journal, 39 (4), pp. 605-610, 2001
- <sup>9</sup>Ma, Y., and Zhong, X. *Receptivity of a supersonic boundary layer over a flat plate, Part 3: Effects of different types of free-stream disturbances*, Journal of Fluid Mechanics 532, 2005
- <sup>10</sup>Balakumar, P. *Receptivity of a supersonic boundary layer to acoustic disturbances*, AIAA Journal 47 (5), 2009, pp. 1069-1078
- <sup>11</sup>Malik, M. R., and Balakumar, P. *Acoustic receptivity of Mach 4.5 boundary layer with leading-edge bluntness*, Theoretical and Computational Fluid Dynamics, 21 (5), 2007, pp. 323-342
- <sup>12</sup>Kara, K., Balakumar, P., and Kandil, O. A. *Receptivity of Hypersonic Boundary Layers Due to Acoustic Disturbances over Blunt Cone*, AIAA Pap. 945, 2007
- <sup>13</sup>Egorov, I. V., Sudakov, V. G., and Fedorov, A. V. *Numerical modeling of the receptivity of a supersonic boundary layer to acoustic disturbances*, Fluid Dynamics 41 (1), 2006
- <sup>14</sup>Cerminara, A., and Sandham, N. *Boundary-layer receptivity and breakdown in hypersonic flow over a swept blunt wedge with three-dimensional freestream acoustic disturbances*, AIAA 2016-4247, 8th AIAA Flow Control Conference, 2016
- <sup>15</sup>Cerminara, A. and Sandham, N.D., 2017. Acoustic leading-edge receptivity for supersonic/hypersonic flows over a blunt wedge. AIAA Journal, 55(12), pp.4234-4244.
- <sup>16</sup>Sawant, S.S., Theofilis, V. and Levin, D.A., 2022. On the synchronisation of three-dimensional shock layer and laminar separation bubble instabilities in hypersonic flow over a double wedge. Journal of Fluid Mechanics, 941.
- <sup>17</sup>Sawant, S.S., Levin, D.A. and Theofilis, V., 2021. Analytical prediction of low-frequency fluctuations inside a one-dimensional shock. Theoretical and Computational Fluid Dynamics, pp.1-16.
- <sup>18</sup>Sawant, S.S., Levin, D.A. and Theofilis, V., 2021. A kinetic approach to studying low-frequency molecular fluctuations in a one-dimensional shock. Physics of Fluids, 33(10), p.104106.
- <sup>19</sup>Fedorov, A. and Tumin, A., 2017. Receptivity of high-speed boundary layers to kinetic fluctuations. AIAA journal, 55(7), pp.2335-2348.

<sup>20</sup>Tumuklu, O., Theofilis, V. and Levin, D.A., 2018. On the unsteadiness of shock–laminar boundary layer interactions of hypersonic flows over a double cone. *Physics of Fluids*, 30(10), p.106111.

<sup>21</sup>Cerminara, A. and Sandham, N., 2020. Transition mechanisms in cross-flow-dominated hypersonic flows with free-stream acoustic noise. *Journal of Fluid Mechanics*, 896.

<sup>22</sup>Klothakis, A., Quintanilha, H., Sawant, S.S. et al. Linear stability analysis of hypersonic boundary layers computed by a kinetic approach: a semi-infinite flat plate at 4.5M94.5M9. *Theor. Comput. Fluid Dyn.* 36, 117–139 (2022). <https://doi.org/10.1007/s00162-021-00601-y>

<sup>23</sup>Yee, H. C., Sandham, N. D., and Djomehri, M. J. *Low-dissipative high-order shock-capturing methods using characteristic-based filters*, *Journal of Computational Physics* 150 (1), pp. 199-238, 1999

<sup>24</sup>De Tullio, N., Paredes, P., Sandham, N. D., and Theofilis, V. *Laminar-turbulent transition induced by a discrete roughness element in a supersonic boundary layer*, *Journal of Fluid Mechanics* 735, pp. 613-646, 2013

<sup>25</sup>Katzer, E., 1989. On the length scales of laminar shock/boundary-layer interaction. *Journal of Fluid Mechanics*, 206, pp.477-496.